Journal of Fluids and Structures 17 (2003) 855–874

JOURNAL OF
FLUIDS AND
STRUCTURES

www.elsevier.nl/locate/jnlabr/yjfls

Simulation of dynamic stall for a NACA 0012 airfoil using a vortex method

M.H. Akbari, S.J. Price*

Department of Mechanical Engineering, McGill University, 817 Sherbrooke St. West, Montréal, Québec, Canada H3A 2K6

Received 26 September 2001; accepted 6 January 2003

Abstract

The unsteady, incompressible, viscous laminar flow over a NACA 0012 airfoil is simulated, and the effects of several parameters investigated. A vortex method is used to solve the two-dimensional Navier–Stokes equations in the vorticity/stream-function form. By applying an operator-splitting method, the "convection" and "diffusion" equations are solved sequentially at each time step. The convection equation is solved using the vortex-in-cell method, and the diffusion equation using a second-order ADI finite difference scheme. The airfoil profile is obtained by mapping a circle in the computational domain into the physical domain through a Joukowski transformation. The effects of several parameters are investigated, such as the reduced frequency, mean angle of attack, location of pitch axis, and the Reynolds number. It is observed that the reduced frequency has the most influence on the flow field.

---

1. Introduction

Stall of an airfoil is characterized by a sudden drop in its normal force following an increase in the angle of attack that causes flow separation. Dynamic stall, on the other hand, is an unsteady phenomenon, where the airfoil pitches through the static stall angle, while the normal force continues to increase beyond its maximum value for unstalled conditions. This phenomenon is often associated with the formation of a leading-edge vortex, called the dynamic stall vortex, that travels along the airfoil surface as it grows, and finally separates from the airfoil at its trailing edge. However, some researchers (e.g., Jumper and Huge, 1991) attribute this lift overshoot to a delay in separation at high incidence, rather than the formation and subsequent convection of the dynamic stall vortex.

The dynamic stall phenomena was first encountered in the helicopter industry, where large torsional oscillations of the blades was observed and attributed to the periodic stalling and unstalling of each blade on the retreating side of the rotor disk. This was considered to be a serious problem, limiting the forward speed and gross weight of the helicopter (Crimi, 1973). This phenomenon may also occur, for example, on axial-flow compressor blades, large wind-mill rotors, or the wings of modern fighters during fast-pitching maneuvers.

Examples of early analytical studies of unsteady airfoil stall can be found in Carta (1967a, b), Ericsson (1967), and Ericsson and Reding (1971). Ericsson and Reding (1972) analyzed the dynamic stall of a helicopter blade section using a quasi-steady theory. Static experimental data were used as input to predict the dynamic stall characteristics of the airfoil; hence, the applicability of this theory was limited by the availability of the required static experimental data. They found the technique to be successful so long as the reduced frequency, $\kappa \equiv \pi f_o c/U_\infty$, was not high ($\kappa < 0.5$), where f_o, c, and U_∞ are the oscillation frequency, chord length, and free-stream velocity, respectively. Further improvements and modifications to their method can be found, for example, in Ericsson and Reding (1980, 1988).

---

*Corresponding author.

E-mail address: stuart.price@mcgill.ca (S.J. Price).

0889-9746/03/$ - see front matter © 2003 Elsevier Science Ltd. All rights reserved.
doi:10.1016/S0889-9746(03)00018-5

McCroskey et al. (1976) experimentally studied dynamic stall, and the associated unsteady boundary layer separation, in incompressible flow at high Reynolds numbers on leading-edge-modified NACA 0012 airfoils. They found the Reynolds number to have a small effect on the normal force and pitching moment coefficients, C_n and C_m. On the other hand, the effects of reduced frequency and leading-edge profile of the airfoil were found to be major. An experimental investigation was performed by Lorber and Carta (1988) to study dynamic stall aerodynamics of an airfoil at *constant pitch rate* and high Reynolds number (up to 4×10^6). It was observed that the strength of the dynamic stall vortex increased with pitch rate, and decreased with increasing Mach number. The *starting flow* over a NACA 0012 airfoil oscillating at large incidences was investigated by Ohmi et al. (1991), using flow visualization experiments and numerical calculations. Reynolds numbers from 1500 to 10^4, and reduced frequencies (in this case, $f^* = fc/2U_\infty$) of 0.1–1.0 were considered. The reduced frequency was identified as a key parameter in determining the vortex wake pattern of the oscillating airfoil. Reynolds number effects were found to be small compared to other parameters. Raffel et al. (1995) investigated the flow field over a NACA 0012 airfoil oscillating in pitch in a low-speed wind tunnel by means of particle image velocimetry (PIV). During the upstroke a dynamic stall vortex formed at the leading edge, which at $\alpha = 24^\circ$, for example, extended over 75% of the upper surface of the airfoil. They observed a strong aperiodicity of the flow structure during the downstroke motion from cycle to cycle.

In the simulations presented here, the dynamic stall characteristics of a pitching NACA 0012 airfoil at Reynolds numbers of 3000 and 10^4 are studied using a vortex method for laminar flows, and the effects of the reduced frequency, mean angle of attack, and location of the pitch axis are investigated.

2. Solution method

The governing equations for the incompressible flow of a Newtonian fluid in two dimensions are the Navier–Stokes and continuity equations, which can be expressed in terms of the vorticity and stream-function as the following

$$\frac{\partial \omega}{\partial t} + (\mathbf{u} \cdot \nabla)\omega = v\nabla^2\omega, \tag{1}$$

$$\nabla^2\psi = -\omega. \tag{2}$$

In these equations $\mathbf{u} = (u, v)$ is the velocity vector, v is the kinematic viscosity, and ω and ψ are the vorticity and stream-function, respectively. Eq. (2) is the Poisson equation for stream-function which replaces the continuity equation.

Following Chorin (1973), an "operator-splitting" method is applied to the governing equations, and the following two equations are obtained, which are solved sequentially in each time step

$$\frac{\partial \omega}{\partial t} = -(\mathbf{u} \cdot \nabla)\omega, \tag{3}$$

$$\frac{\partial \omega}{\partial t} = v\nabla^2\omega. \tag{4}$$

In this study, the vorticity field is discretized into a number of point vortices, and the time domain is also discretized into small time steps. Eq. (3) states that the total derivative of vorticity is zero during "convection", or that the vorticity of a particle is constant as it is convected with the local velocity. Hence, in order to satisfy the "convection" part of the governing equations, the velocity field is obtained, and each "vortex particle" is convected with the local velocity for the period of the time step. To do that, Eq. (2) is solved for the stream-function (given the vorticity field), and the velocity field is then computed as the curl of the stream function. Next, the diffusion process is simulated by solving Eq. (4) using a second-order ADI finite difference scheme. The "no-flow" boundary condition is satisfied during the solution of the convection problem, and the "no-slip" boundary condition is satisfied by the creation of new vorticity on the body surface during each time step.

In the present vortex method, a computational grid is used for the following purposes: (a) solving the Poisson equation for the stream-function given the vorticity field, (b) calculating the velocity field given the stream-function, (c) solving the diffusion equation for the vorticity field. Also, the new vorticity is created at the location of the first row of grid nodes, on the surface of the body. The computational grid is fixed to the body, and hence, moves with the airfoil as it oscillates.

Further specific details of the numerical methods used in this study (including derivation of equations, accuracy of the numerical schemes, the computational grid, and calculation of the force coefficients) are given in Akbari and Price (2000) and Akbari (1999), and hence are not repeated here for the sake of brevity. It is noted here, however, that the present vortex method is applicable only to two-dimensional, incompressible flows, the numerical schemes are unconditionally stable, and the finite-difference formulations (for the solution of the Poisson and diffusion equations) are nominally second-order accurate.

In this study, a pitching airfoil is considered, with the instantaneous angle of attack given by

$$\alpha = \bar{\alpha} + A\cos(\Omega t), \tag{5}$$

where α is the angle of attack at time t, $\bar{\alpha}$ is the mean angle of attack, A is the amplitude of the pitching oscillation (in rad), and $\Omega = 2\pi f$, with f being the frequency of oscillation.

3. Airfoil profile

In this study, conformal transformations are used to map a circle onto an airfoil, and vice versa. The general form of the transformation $\mathscr{F} : \mathbf{z}(x, y) \rightarrow \mathbf{w}(\xi, \eta)$ that transforms a circle onto our desired profile is given by

$$w = \mathscr{F}(z) = \left[\left(z + \frac{(C-B)^2}{z}\right) - P\right]\mathrm{e}^{-\mathrm{i}\alpha} + P, \tag{6}$$

where $z = x + \mathrm{i}y$ is a point on or outside the circle in the $\mathbf{z}$-plane, $w = \xi + \mathrm{i}\eta$ is the corresponding point on or outside the transformed profile in the $\mathbf{w}$-plane, and B, C, α, and P are control parameters that are described below with the help of Fig. 1.

As can be seen in Fig. 1, C is the interception point of the circle and the positive side of the x-axis. The center of the circle is located at point $(-\varepsilon, \delta)$, P is the location of the rotation axis of the profile in the $\mathbf{w}$-plane, and α is the angle of rotation, positive in the clockwise direction. B in Eq. (6) is a control parameter that, along with the eccentricity of the circle, determines the shape of the profile in the transformed plane ($\mathbf{w}$-plane).

In this article, an airfoil profile is considered that closely resembles the NACA 0012 airfoil, by setting $\varepsilon = 0.068$, $\delta = 0$, and $B = 0.04$ in Eq. (6). The profiles of the airfoil obtained by our transformation and that of a NACA 0012 airfoil are compared with each other in Fig. 2, and, as can be seen, they are indistinguishable from one another. A close-up view of the two profiles in the vicinity of the leading- and trailing-edges is given in Fig. 3. As seen, in these areas the differences between the two profiles are noticeable. However, one should consider the scale of the plots in order to realize the insignificance of these differences between the two profiles. Therefore, we will consider our profile to be a very close resemblance of a NACA 0012 airfoil.

4. Results and discussion

The simulation results from our parameteric study of the dynamic stall flow of the NACA 0012 airfoil are presented here. A summary of the case-studies in this investigation is shown in Table 1. In this work emphasis is put on investigating the effects of reduced frequency of oscillation of the airfoil. In all case-studies the flow is started

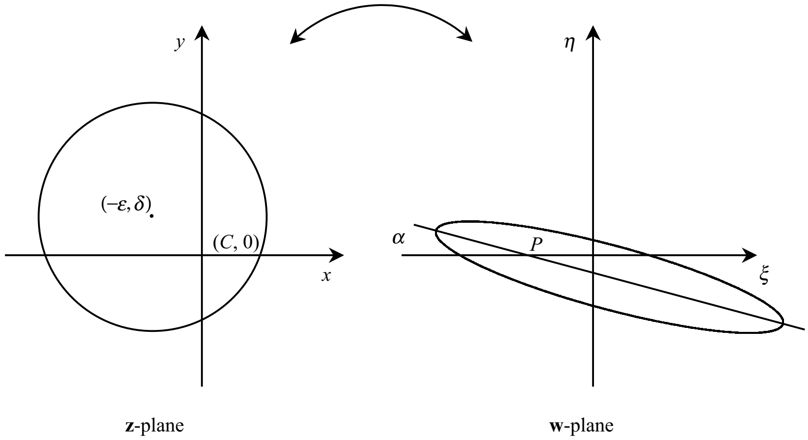

Fig. 1. The Joukowski transformation of the **z**-plane (circle) into the **w**-plane (airfoil).

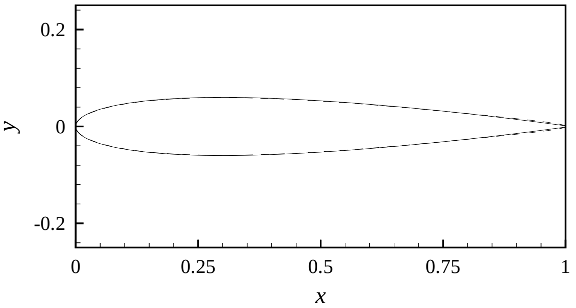

Fig. 2. Comparison of a NACA 0012 airfoil profile and that obtained from our transformation: ——, NACA 0012 profile; - - -, profile from transformation.

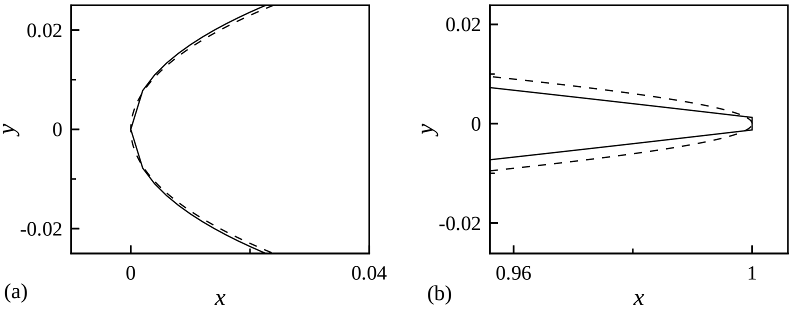

Fig. 3. Close-up view of the two profiles in the vicinity of: (a) the leading-edge, (b) the trailing-edge: ——, NACA 0012 profile; - - -, profile from transformation.

Table 1
Input parameters for simulations of cross-flow over a pitching NACA 0012 airfoil

Re	κ	$\bar{\alpha}$	$\Delta\alpha$	Axis
10^4	0.15	15°	10°	$c/4$
10^4	0.25	15°	10°	$c/4$
10^4	0.50	15°	10°	$c/4$
3000	0.25	15°	10°	$c/4$
10^4	0.25	20°	10°	$c/4$
10^4	0.25	15°	10°	$c/2$

impulsively at a steady angle of attack $\alpha_{\min}$. After the flow achieves steady state at this steady angle, the pitching oscillation of the airfoil is started at the given frequency, and a few oscillation cycles of the airfoil are simulated.

In the following, the force and pitching moment coefficients for all cases are presented and analyzed, and the flow fields are studied. In all numerical simulations a time-step size of $\Delta t = 0.01$ and 300×360 grids have been used. It should be noted that the numerical method used in this study is unconditionally stable, and the selected numerical parameters produced grid-independent results.

4.1. Static airfoil

A number of flow simulations are first presented for steady angles of attack of the airfoil. In this study the static stall angle is predicted at $\alpha \approx 15^\circ$ for a Reynolds number of $\mathrm{Re} = 10^4$. The steady values of the force and pitching moment coefficients versus angle of attack are plotted in Fig. 4. In Fig. 4(a), the normal force coefficient predictions for $\mathrm{Re} = 10^4$ are compared with the experimental results taken from Abbott and von Doenhoff (1959) for $\mathrm{Re} = 6 \times 10^6$,

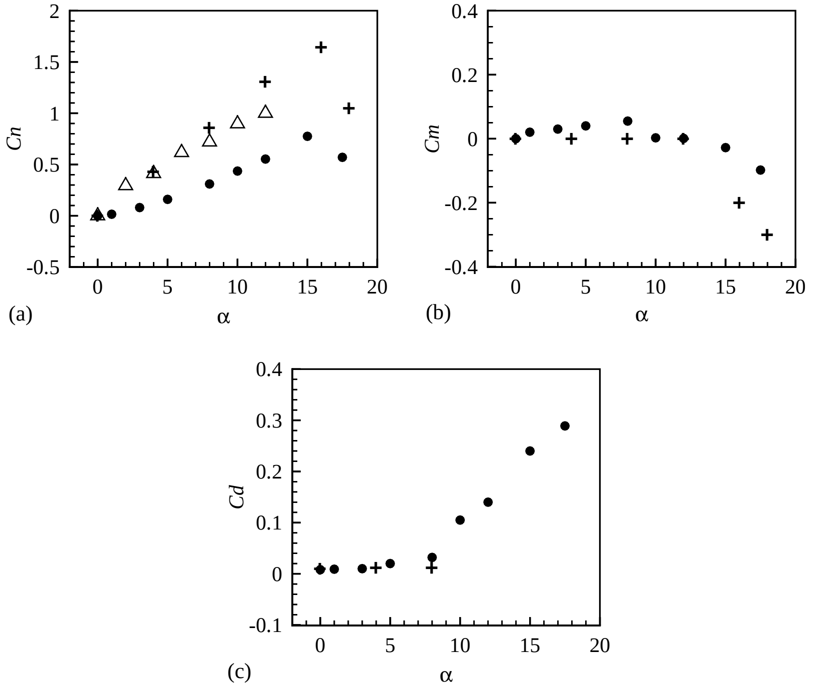

Fig. 4. The force and pitching moment coefficients at steady angles of attack: (a) C_n, (b) C_m, (c) C_d. ● present numerical results for Re $= 10^4$; △ experimental results due to Johari and Durgin (1998) for Re $= 1.02 \times 10^5$; + experimental results from Abbott and von Doenhoff (1959) for Re $= 6 \times 10^6$.

and from Johari and Durgin (1998) for Re $= 1.02 \times 10^5$ (all data are for a NACA 0012 airfoil). As seen in this figure, the flow Reynolds number has some effect on the normal force coefficient. A consistent decrease with decreasing Reynolds number (over a range of two orders of magnitude) is observed in the magnitude of the normal force coefficient. This effect has been reported previously for a large change in the Reynolds number. For example, Massey (1979) presented the static lift and drag coefficients versus angle of attack for a particular airfoil at two Reynolds numbers of 4.3×10^5 and 2.1×10^4, where for any given angle C_l is considerably lower at the lower Reynolds number (e.g., at $\alpha = 10°$, 0.49 compared to 1.4), and C_d is higher (e.g., at $\alpha = 10°$, 0.19 compared to 0.07). By comparison, Fig. 4(a) shows a reasonable agreement of our numerical results with the experimental data, considering the differences in the Reynolds number. The static stall occurs at $\alpha \approx 16°$ in the experiments reported by Abbott and von Doenhoff, and it is predicted at $\alpha \approx 15°$ in this study.

As seen in Fig. 4(b), the pitching moment coefficient (around the quarter-chord) in the experimental data is approximately zero for $\alpha \leqslant 12°$, and then it drops to negative values at higher angles of attack. However, in our simulations the pitching moment coefficient is predicted at positive values for some angles of attack of less than 12°; nonetheless, the trend in our data follows that in the experimental data for $\alpha \geqslant 12°$. The differences in the magnitude of the moment coefficient for $\alpha > 12°$ are attributed to the large difference in the Reynolds number. Note that the normal force coefficient is lower at a lower Reynolds number, hence, with similar locations for the aerodynamic center, a lower pitching moment coefficient is expected at a lower Reynolds number.

Shown in Fig. 4(c) are the calculated drag coefficients in this study, along with some experimental data from Abbott and von Doenhoff (1959). No experimental data for C_d is available for $\alpha > 8°$. The scale of this plot is too large for the variation of experimental C_d with α to be clearly seen. Our numerical results also predict small values for C_d at $\alpha \leqslant 8°$, followed by a considerable increase at higher angles of attack. The drag coefficient predicted in the present study has a higher magnitude than that reported from experiments for $\alpha \leqslant 8°$, where experimental data are available. However, note should be made that these data are for Reynolds numbers of two orders of magnitude difference. A higher drag coefficient is expected at a lower Reynolds number for the same airfoil at the same angle of attack (e.g., Massey, 1979).

Overall, the simulation results from this study for steady angles of attack are in reasonable agreement with available experimental data (considering the Reynolds number differences), particularly in terms of the lift coefficient and the static stall angle.

4.2. A flow visualization comparison

Before presenting the flow field results for the main case-studies, we shall first study a case for which some experimental flow visualization results are available.

Ohmi et al. (1991) studied the *starting flow* over a NACA 0012 airfoil for Reynolds numbers of between 1500 and 10^4, and at different reduced frequencies. Shown in Fig. 5 are their experimental flow visualization results for the streamline patterns of the unsteady flow past the pitching airfoil with[1] $\kappa = 0.2\pi$, $\mathrm{Re} = 3000$, $\bar{\alpha} = 30°$, $\Delta\alpha = 15°$, $\alpha_0 = 15°$, and $x/c = 0.5$. The pitching oscillation of the airfoil started from the minimum incidence with the impulsive start of the flow, and one oscillation cycle was completed during the experiment. As can be seen in the figure, the flow remains attached to the airfoil up to dimensionless time $t^* \equiv tU_\infty/c = 1$ after the impulsive start, when $\alpha \approx 25°$. Then, the flow starts to separate from the leading-edge, and a leading-edge vortex forms, grows, and is eventually shed from the upper surface some time later during the downstroke. During the remainder of the oscillation cycle smaller vortex structures are shed from both the upper surface and the trailing-edge of the airfoil.

The streamline plots from our simulation of the same flow as that studied by Ohmi et al. are presented in Fig. 6. Each part of this figure corresponds to the similar part of Fig. 5. The two sets of plots are in a very good agreement, especially for times up to $t^* = 1.5$. At this time the flow starts to separate from the airfoil, with the formation of a leading-edge vortex. The size of this vortex at $t^* = 2$ is larger in the experimental results compared to that predicted in our simulation, as seen in parts (d) of the two figures. The overall structure of the flow field is still very similar at $t^* = 3$, including the wavy streamlines originating from the trailing-edge. As seen in parts (g) of the figures, the size and position of the trailing-edge vortex at $t^* = 3.5$ are very similar in the two sets of results. The formation of a trailing-edge vortex from $t^* = 4$ to 4.5 can be seen in both set of plots.

Overall, a high degree of similarity is observed between our simulation results for the flow field and those from the experiment. This serves as a validation of the accuracy of the results obtained from our numerical simulations.

4.3. Dynamic stall flow

4.3.1. Effect of reduced frequency

Shown in Fig. 7 are the normal force (C_n), pitching moment (C_m), and drag (C_d) coefficients during five oscillation cycles of the airfoil at $\bar{\alpha} = 15°$, with $\Delta\alpha = 10°$ and a reduced frequency of 0.5, at $\mathrm{Re} = 10^4$. As seen in the figure, after completion of the second cycle no transient effects are present in the hysteresis loops; the differences that exist from one cycle to the next after the second cycle of oscillation are due to the unsteady nature of the flow. Hence, it is believed that simulating even fewer number of oscillation cycles would still capture the overall characteristics of the flow field.

Shown in Fig. 8 are the normal force, pitching moment, and drag coefficients, averaged over the last two oscillation cycles as a function of reduced frequency, along with the variation of the same coefficients for steady angles of attack. It is observed that the normal force coefficient in the pitching cases increase well beyond that at the static stall. Note that stall occurs at $\alpha \approx 15°$ in the steady case, when the normal force coefficient is $C_n \approx 0.77$.

Hysteresis effects are observed in the force and pitching moment coefficients at all reduced frequencies. At the lowest reduced frequency, $\kappa = 0.15$, stall occurs at $\alpha \approx 21.5°$. In this case an overall positive damping in the pitching moment loop is observed. This is concluded by comparing the areas of clockwise and counter-clockwise loops in the plot of the pitching moment versus angle of attack. When the frequency is increased to $\kappa = 0.25$ stall is delayed to $\alpha_{\max} = 25°$, and the positive-damping area in the pitching moment loop decreases compared to that obtained with $\kappa = 0.15$. When the reduced frequency is increased further to $\kappa = 0.5$ the net damping in the pitching moment loop becomes negative. In this case the drag coefficient loop is narrower, and the normal force coefficient takes negative values during the downstrokes.

By comparing the results of these three case-studies, it is concluded that increasing the reduced frequency can slightly increase the normal force "overshoot" up to a limit of 1.6, after which any further increase in the reduced frequency has no apparent effect on the "overshoot". However, an increase in the reduced frequency also modifies the general profile of the hysteresis loops. The minimum normal force coefficient decreases, and the drag coefficient loop becomes narrower with increasing reduced frequency. But, perhaps the most important effect of increasing the reduced frequency is the significant increase of the negative damping in the pitching moment cycle. Reducing negative damping in the pitching moment cycle of the airfoil is important in the stability of its torsional oscillations.

In order to validate our numerical results for the force coefficients of a pitching airfoil a comparison with some experimental results, or other reliable numerical data, is desirable. However, all the available experimental and numerical results for the dynamic stall flow that also include the measurement or calculation of force coefficients, cover

---

[1] Note that $\kappa = 0.2\pi$ is higher than that of the other results presented in this paper.

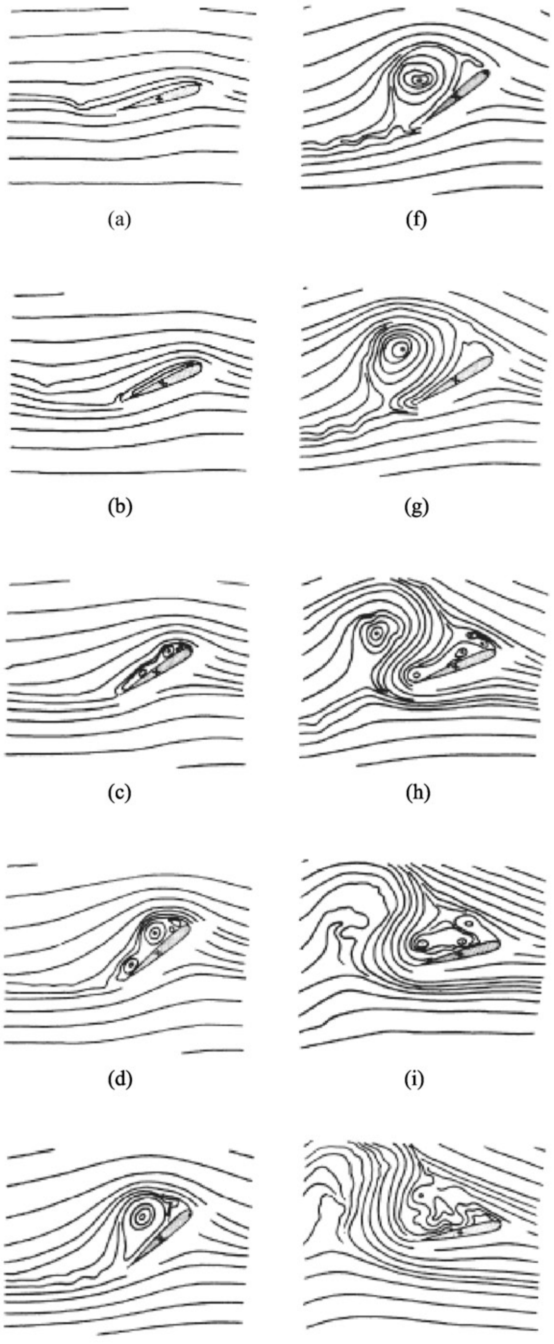

Fig. 5. Streamline plots for the NACA 0012 airfoil at Re = 3000, $f^* = 1.0$, $\bar{\alpha} = 30°$, $\Delta\alpha = 15°$, and $\alpha_0 = 15°$, taken from Ohmi et al. (1991). (a) $t^* = 0.5$, $\alpha = 17.9°$; (b) $t^* = 1.0$, $\alpha = 25.4°$; (c) $t^* = 1.5$, $\alpha = 34.6°$; (d) $t^* = 2.0$, $\alpha = 42.1°$; (e) $t^* = 2.5$, $\alpha = 45.0°$; (f) $t^* = 3.0$, $\alpha = 42.1°$; (g) $t^* = 3.5$, $\alpha = 34.6°$; (h) $t^* = 4.0$, $\alpha = 25.4°$; (i) $t^* = 4.5$, $\alpha = 17.9°$; (j) $t^* = 5.0$, $\alpha = 15.0°$.

the turbulent flow regime, at high Reynolds numbers of at least 10^6. Our numerical method, being for a laminar regime, is not expected to produce accurate results for Reynolds numbers of higher than about 10^4. This large difference in the Reynolds number (10^4 versus 10^6) has considerable effects on the behavior of the flow field and the force coefficients.

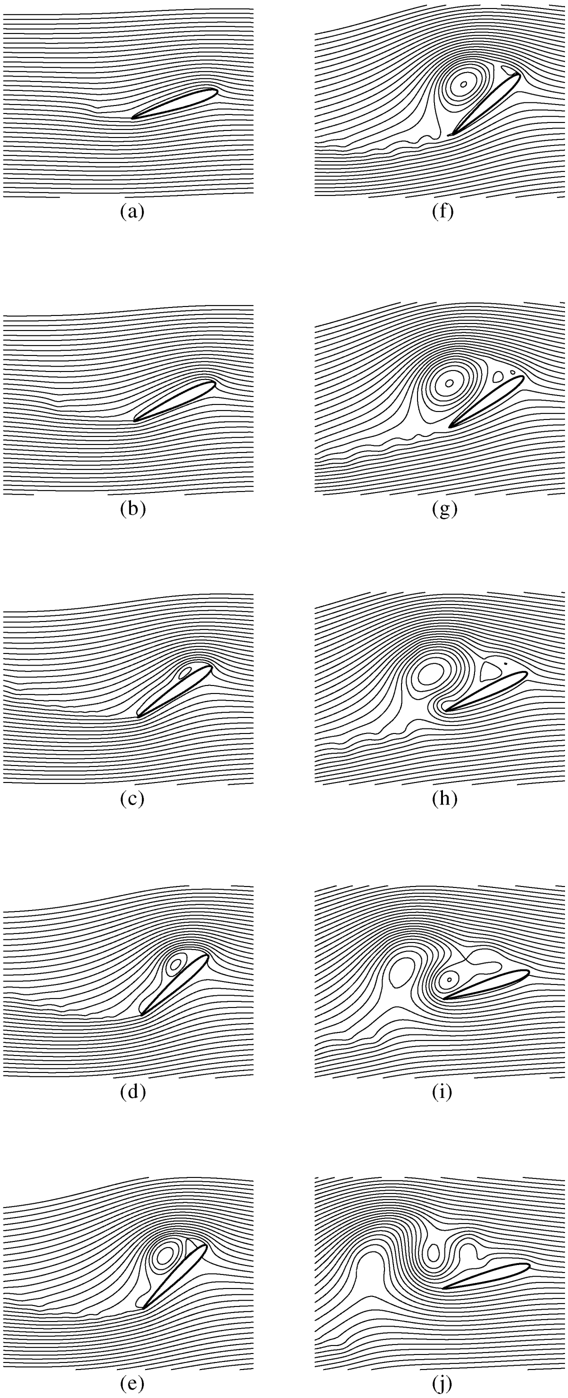

(a) (f)

(b) (g)

(c) (h)

(d) (i)

(e) (j)

Fig. 6. Streamline plots for the NACA 0012 airfoil at Re $= 3000$, $f^* = 1.0$, $\bar{\alpha} = 30°$, $\Delta\alpha = 15°$, and $\alpha_0 = 15°$, from our simulation. (a) $t^* = 0.5$, $\alpha = 17.9°$; (b) $t^* = 1.0$, $\alpha = 25.4°$; (c) $t^* = 1.5$, $\alpha = 34.6°$; (d) $t^* = 2.0$, $\alpha = 42.1°$; (e) $t^* = 2.5$, $\alpha = 45.0°$; (f) $t^* = 3.0$, $\alpha = 42.1°$; (g) $t^* = 3.5$, $\alpha = 34.6°$; (h) $t^* = 4.0$, $\alpha = 25.4°$; (i) $t^* = 4.5$, $\alpha = 17.9°$; (j) $t^* = 5.0$, $\alpha = 15.0°$.

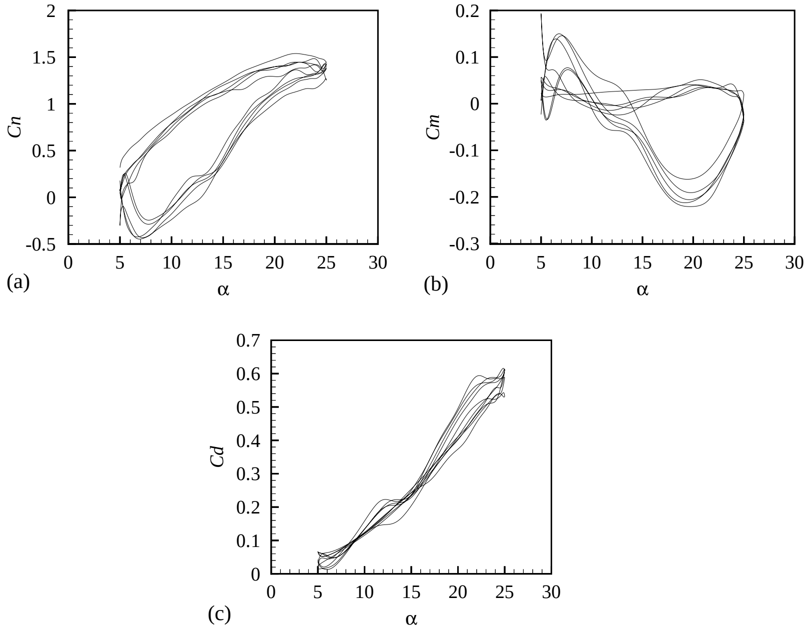

Fig. 7. The force and pitching moment coefficients versus angle of attack over five oscillation cycles for the airfoil at $\bar{\alpha} = 15^\circ$, $\Delta\alpha = 10^\circ$, $\kappa = 0.5$, $\mathrm{Re} = 10^4$; (a) C_n, (b) C_m, (c) C_d.

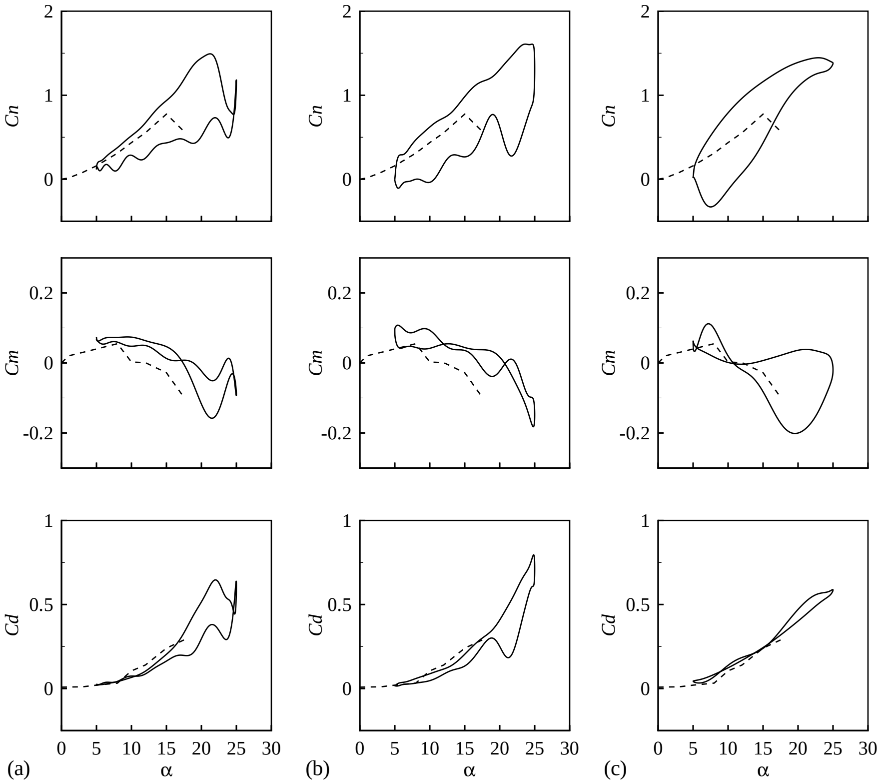

Fig. 8. The hysteresis loops for the normal force (C_n), pitching moment (C_m), and drag (C_d) coefficients for the airfoil at $\bar{\alpha} = 15^\circ$ and $\mathrm{Re} = 10^4$ oscillating with $\Delta\alpha = 10^\circ$, $x/c = 0.25$, and reduced frequency: (a) 0.15, (b) 0.25, (c) 0.5: ——, pitching case; - - -, steady case.

Hence, a *qualitative* comparison is made between our calculated force coefficients and a set of reliable data at the lowest Reynolds number available to us.

Presented in Fig. 9 is a qualitative comparison of our results for $\kappa = 0.15$ and 0.25, $\bar{\alpha} = 15°$, and $\Delta\alpha = 10°$, with the numerical results due to Tuncer et al. (1990) for the dynamic stall of the same airfoil at $\mathrm{Re} = 10^6$ oscillating at the same frequencies and angles of attack. Note that no data for C_d are presented in Tuncer et al. (1990) for the case with $\kappa = 0.25$.

Some differences are observed between the two sets of results. Higher values of C_n and lower values of C_d are reported for $\mathrm{Re} = 10^6$ compared to our calculated results for $\mathrm{Re} = 10^4$. This behavior was expected due to the Reynolds number difference. Stall is predicted at $\alpha \approx 21.5°$ in our simulation for $\kappa = 0.15$, while no stall is observed for this case at $\mathrm{Re} = 10^6$. Because of this, a minimum value for C_m is obtained at $\alpha \approx 21.5°$ in our calculations, while at $\mathrm{Re} = 10^6$ C_m continues decreasing with decreasing α. However, for $\kappa = 0.25$ no stall effects are observed in the C_n loop in either study. This is evident from the shape of the loops where C_n continues to increase with α up to the maximum angle of attack. It is interesting to see the negative-damping region in the C_m loop reported in Tuncer's results for $\kappa = 0.25$. The same behavior is observed at a higher reduced frequency of $\kappa = 0.5$ in our simulations for $\mathrm{Re} = 10^4$.

It seems that our results for $\kappa = 0.25$ and 0.5 are, respectively, more similar to Tuncer's numerical results for $\kappa = 0.15$ and 0.25. This observation suggests that a Reynolds number increase can also intensify the effects of the reduced

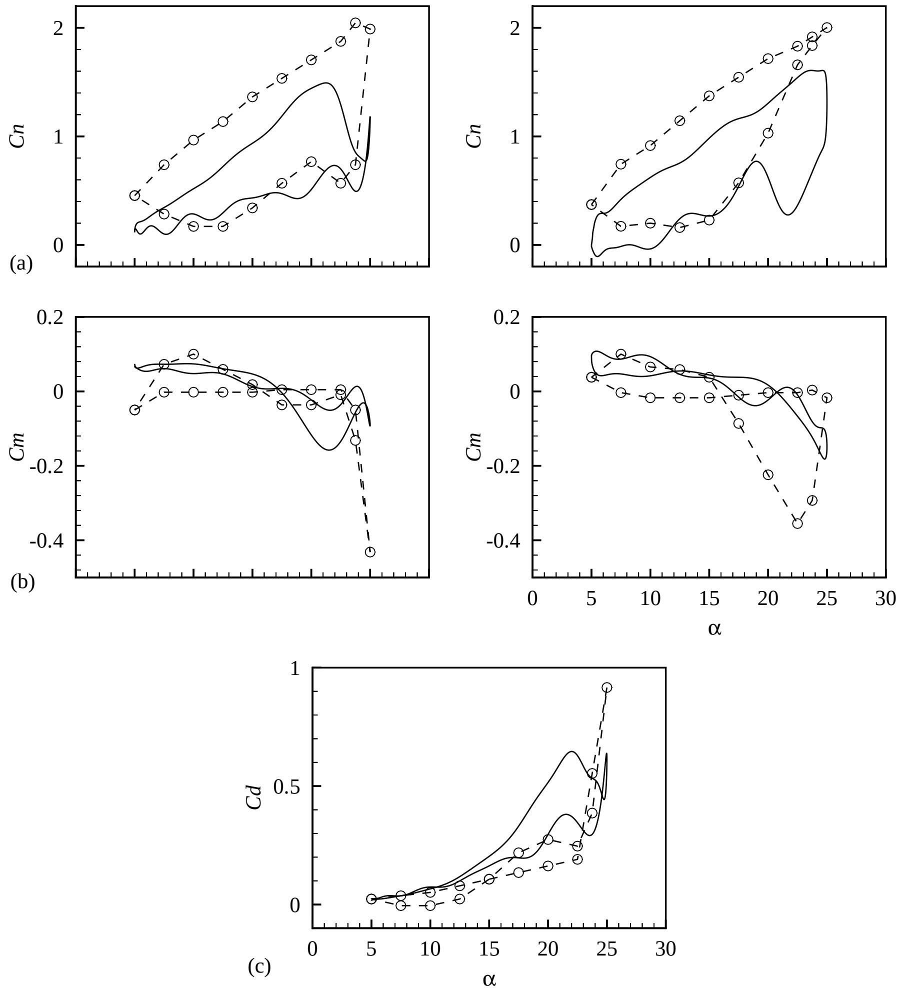

Fig. 9. Comparison of the hysteresis loops for the force and pitching moment coefficients of the NACA 0012 airfoil oscillating about $c/4$ between $\alpha = 5°$ and 25°: ——, our numerical results for $\mathrm{Re} = 10^4$; –○– –○–, numerical results due to Tuncer et al. (1990) for $\mathrm{Re} = 10^6$. (a) C_n, (b) C_m, (c) C_d: on the left $\kappa = 0.15$, on the right $\kappa = 0.25$.

frequency. Overall, despite such a large difference in the Reynolds number, some quantitative agreement is observed between the two sets of results in terms of the hysteresis loops.

The flow field development for one cycle of oscillation of the airfoil is now presented for each case-study considered so far. In the vorticity contour plots that follow, the white and black areas indicate positive and negative vorticity, respectively.

Shown in Fig. 10 are a sequence of vorticity contour plots for the flow around the airfoil at several angles of incidence during the third cycle of oscillation of the airfoil at $\bar{\alpha} = 15^\circ$, with $\Delta\alpha = 10^\circ$ and a reduced frequency of 0.15, at $\mathrm{Re} = 10^4$. No apparent indication of flow separation is observed on the airfoil up to $\alpha \approx 13.6^\circ$ (Fig. 10d). At $\alpha \approx 16.7^\circ$ a leading-edge separation bubble starts forming on the airfoil. Because of the relatively small scale of the vorticity contour shown in Fig. 10(e), this separation bubble is not easily seen; however, the separation bubble is apparent when larger scale versions of this figure are examined. Note that static stall occurs at $\alpha \approx 15^\circ$. The separation bubble is seen to cover most of the upper surface of the airfoil when $\alpha \approx 19^\circ$ (Fig. 10f). At $\alpha \approx 22^\circ$ the leading-edge vortex is shed from the airfoil. At the maximum incidence $\alpha = 25^\circ$ a vortex forms at the trailing-edge, that promotes the separation of the leading-edge vortex.

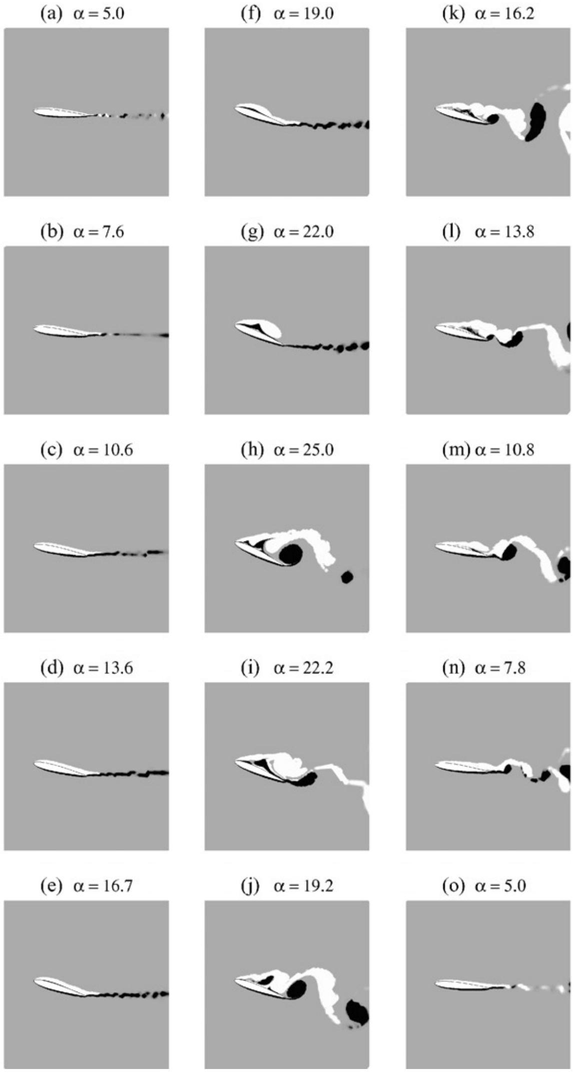

Fig. 10. Vorticity contour plots at several angles of attack for a pitching NACA 0012 airfoil, at $\kappa = 0.15$, $\Delta\alpha = 10^\circ$, $\bar{\alpha} = 15^\circ$, rotation axis at $c/4$, and $\mathrm{Re} = 10^4$.

During the downstroke the trailing-edge vortex is shed, and a new leading-edge vortex grows and is about to be shed when $\alpha \approx 22.2^\circ$. In parts (j) to (m) of the figure two other smaller trailing-edge vortices can be seen shedding during the downstroke. In the mean time, two vortical structures (with opposite rotation to the trailing-edge vortices) are also shed from the upper surface of the airfoil. When α reaches $\approx 7.8^\circ$ during the downstroke the flow is already attached at the leading-edge, and by the time the cycle is complete the flow is reattached over the entire surface of the airfoil.

Fig. 8(a) shows that the normal force coefficient in this case continues to increase during the upstroke up to $\alpha \approx 21^\circ$. This is the point at which flow separates from the airfoil, as seen in Fig. 10(e)–(g). Near the maximum incidence, the normal force suddenly increases again; this is due to the trailing-edge vortex being formed completely and giving a suction effect over large part of the upper surface. During the downstroke, till $\alpha \approx 7.8^\circ$, the normal force coefficient is smaller than during the upstroke; this is attributed to the flow separation during this part of the cycle. Near the end of the downstroke the normal force increases again, this is coincident with flow reattachment on the upper surface.

The vorticity contour plots for the airfoil at $\bar{\alpha} = 15^\circ$, $\Delta\alpha = 10^\circ$, and $\kappa = 0.25$ are shown for the third oscillation cycle in Fig. 11. At the beginning of the cycle the flow is not completely attached to the surface, and there are vortices in the

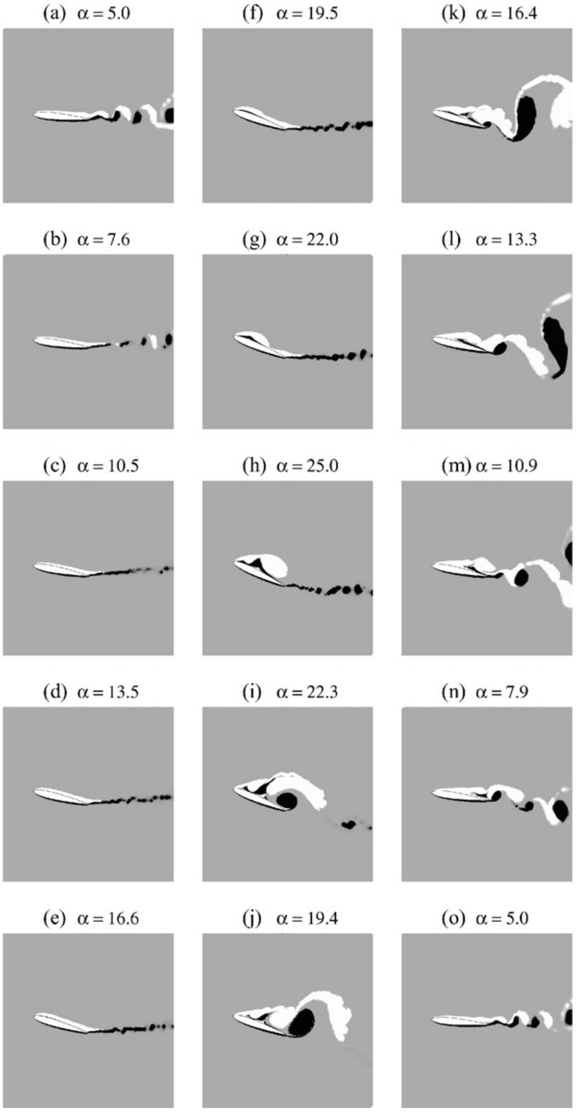
(a) $\alpha = 5.0$
(b) $\alpha = 7.6$
(c) $\alpha = 10.5$
(d) $\alpha = 13.5$
(e) $\alpha = 16.6$
(f) $\alpha = 19.5$
(g) $\alpha = 22.0$
(h) $\alpha = 25.0$
(i) $\alpha = 22.3$
(j) $\alpha = 19.4$
(k) $\alpha = 16.4$
(l) $\alpha = 13.3$
(m) $\alpha = 10.9$
(n) $\alpha = 7.9$
(o) $\alpha = 5.0$

Fig. 11. Vorticity contour plots at several angles of attack for a pitching NACA 0012 airfoil, at $\kappa = 0.25$, $\Delta\alpha = 10^\circ$, $\bar{\alpha} = 15^\circ$, rotation axis at $c/4$, and $\mathrm{Re} = 10^4$.

near wake which are due to the separation and vortex shedding from the previous cycle. As time increases the flow becomes fully attached to the surface and the small vortices in the wake are convected downstream. The flow remains fully attached to the surface up to $\alpha \approx 16.5^\circ$. At $\alpha \approx 19.5^\circ$ the flow starts to separate from the leading-edge, and at $\alpha \approx 22^\circ$ the flow is fully separated with the leading-edge vortex being fully formed and covering two-thirds of the upper surface. Note that in the previous case, $\kappa = 0.15$, this situation was observed at $\alpha \approx 19.3^\circ$. At $\alpha_{\max}$ the leading-edge vortex is shed from the airfoil at about mid-chord position on the upper surface. Later during the downstroke at $\alpha \approx 22.3^\circ$ a trailing-edge vortex is formed while the leading-edge vortex is being convected in the near wake. The flow over the upper surface and in the wake remain vortical during the downstroke, as two smaller vortices from the trailing-edge and other vortical structures from the upper surface are shed. At the end of the cycle the flow reattaches to most of the upper surface. Note the similarities in the flow field between the beginning and the end of the cycle.

It is interesting to note that the flow field remains "quiet" during most of the upstroke, and much of the separation and vortex-shedding activity occurs between $\alpha \approx 22^\circ$ in the upstroke and $\alpha \approx 8^\circ$ in the downstroke. Also interesting to note is the speed at which the flow field changes near $\alpha_{\max}$ in the upstroke. During a change in incidence of only about 3°, from $\alpha \approx 22^\circ$ to 25°, the flow field "bursts" into a vortical flow and remains as such in the downstroke down to $\alpha \approx 7^\circ$.

As seen in the normal force coefficient plot for this case, Fig. 8(b), C_n continues to increase up to $\alpha_{\max}$ during the upstroke; that is when the flow completely separates from the surface. In this case the flow separates at a higher incidence compared to the previous case with a lower reduced frequency, $\kappa = 0.15$. Also, similar to the previous case, both the separation and reattachment of the flow start from the leading-edge.

Shown in Fig. 12 are the vorticity contour plots for the airfoil at $\bar{\alpha} = 15^\circ$, $\Delta\alpha = 10^\circ$, and $\kappa = 0.5$ during the third oscillation cycle. At the beginning of the cycle the wake is still vortical and the flow remains separated over the rear half of the upper surface of the airfoil as a result of separation in the previous cycle. In this case the frequency of oscillation is so high that the flow cannot recover from the separation which occurred in the previous cycle. As time increases the vortices on the airfoil are convected downstream, and the flow becomes attached to the entire upper surface, even though the angle of attack is increasing. This is seen in parts (b)–(e) of the figure for incidences up to $\alpha \approx 16^\circ$. At $\alpha \approx 19^\circ$ the first indication of a leading-edge separation bubble can be observed, but the flow is still attached over most of the surface. At $\alpha \approx 22.4^\circ$ this separation bubble increases in size. Note that the narrow separation region on the rear half of the upper surface is the result of the previous cycle of oscillation, and is not due to the newly formed separation bubble. At $\alpha = 25^\circ$ the leading-edge vortex has completely formed and has travelled half-way along the surface. This should be compared with the previous two cases, $\kappa = 0.15$ and 0.25, in which the leading-edge vortex had already travelled further downstream at this angle of attack. The leading-edge vortex continues to evolve and travel downstream during the downstroke, down to $\alpha \approx 13.3^\circ$. At $\alpha \approx 10.4^\circ$, as the leading-edge vortex is being shed, a trailing-edge vortex starts to form. During the remainder of the downstroke the trailing-edge vortex continues to grow, and is later shed from the airfoil. This is while the remains of the first leading-edge vortex, and the smaller, secondary vortices formed on the upper surface during the downstroke, prevent the flow from reattaching.

The separated flow at such small angles of attack results in a high-pressure area on the upper surface of the airfoil, such that the lift coefficient takes negative values, as seen in Fig. 8(c). For most of the downstroke the leading-edge vortex covers all of the upper surface aft of the quarter-chord, and hence, the low-pressure region on that part of the airfoil results in a negative pitching moment between $\alpha \approx 25^\circ$ and 12°; see Fig. 8(c). Note the considerable differences in the flow field between this case, with the highest reduced frequency, $\kappa = 0.5$, and the previous two cases, with $\kappa = 0.15$ and 0.25. In the present case the flow remains attached to most of the upper surface during most of the upstroke (Fig. 12b–e), the leading-edge vortex is formed and released entirely during the downstroke, and only one trailing-edge vortex is shed per cycle of oscillation. Also both the separation and reattachment of the flow started from the leading-edge, similar to the previous two cases with lower reduced frequencies.

4.3.2. Effect of Reynolds number

Results for a Reynolds number of $\mathrm{Re} = 3000$, a value about three times lower than in other case-studies, are shown in Fig. 13(a). If these results are compared with those of Fig. 8(b) the effect of Reynolds number can be seen. In general, the hysteresis loops in the two cases are very similar. However, the minimum value of C_m is around -0.14 for $\mathrm{Re} = 3000$, and around -0.19 for $\mathrm{Re} = 10^4$. Also, the area of the negative-damping region near $\alpha_{\max}$ is larger for the lower Reynolds number. Other than these differences in detail, the two sets of hysteresis loops are very similar for these two cases. These results suggest that, compared to other parameters, a Reynolds number difference of this order has only minor effects on the behavior of the force and pitching moment coefficients in the dynamic stall characteristics of this airfoil.

4.3.3. Effect of mean incidence

If the mean incidence is increased to $\bar{\alpha} = 20^\circ$ the resulting force and moment coefficients are as plotted in Fig. 13(b). The force coefficient hysteresis loops suggest that stall occurs at $\alpha \approx 26.5^\circ$. Comparing the results for this case with those for a mean incidence of 15°, Fig. 8(b), shows that an increase in the mean incidence has considerable effect on the force and moment coefficients of a pitching airfoil. In particular, for the results at the higher value of incidence the hysteresis loops are wider (higher hysteresis effects); the maximum value and the average of the force coefficients are greater; and the negative damping in the pitching moment loop is smaller.

The vorticity contour plots during the third oscillation cycle for the airfoil at $\bar{\alpha} = 20^\circ$, $\Delta\alpha = 10^\circ$, and $\kappa = 0.25$ are shown in Fig. 14. At the beginning of the cycle the flow is still separated over parts of the upper surface as a result of the flow separation which occurred during the previous cycle. However, later at $\alpha \approx 12.6^\circ$ the flow reattaches to parts of the surface. At $\alpha \approx 15.5^\circ$ a new separation bubble starts to form on the upper surface of the airfoil. The development of this separation bubble into a vortex is observed during $\alpha \approx 18.5^\circ$ to 24.5°. At $\alpha \approx 27^\circ$ this vortex is about to shed from the surface.

At the maximum incidence of the airfoil a trailing-edge vortex forms, producing a large region of flow separation on the surface. During the downstroke two other trailing-edge vortices form and are shed, while two large-scale structures of positive vorticity form and are released from the upper surface. As the end of the oscillation cycle is approached the

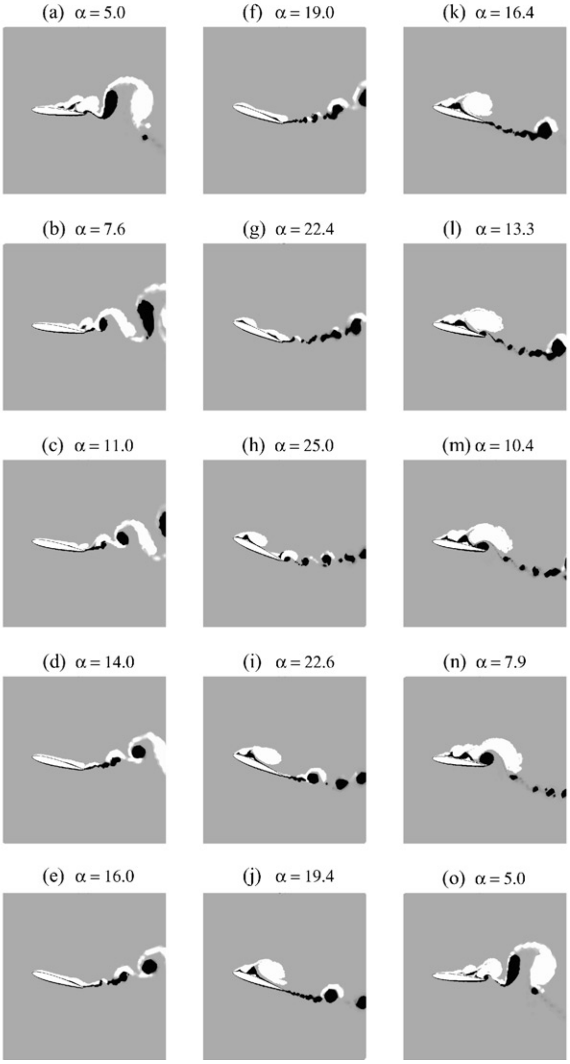

Fig. 12. Vorticity contour plots at several angles of attack for a pitching NACA 0012 airfoil, at $\kappa = 0.50$, $\Delta\alpha = 10^\circ$, $\bar{\alpha} = 15^\circ$, rotation axis at $c/4$, and $\mathrm{Re} = 10^4$.

formation of any further vortices ceases, but the flow remains separated over most of the upper surface. Compared to the simulation with a lower mean incidence $\bar{\alpha} = 15°$, in this case the flow remains separated during a longer period of the oscillation cycle and the wake is more vortical and violent.

As observed in Fig. 14(f) and (g), the flow becomes massively separated at $\alpha \approx 25°$ during the upstroke. This is associated with a steep drop in the normal force coefficient, as shown in Fig. 13(b). Also, referring to Fig. 14(e) and (k), for example, one can explain the behavior of the pitching moment coefficient in the upstroke compared to the downstroke, at $\alpha \approx 21°$. During the upstroke at $\alpha \approx 21°$, shown in Fig. 14(e), there is a large vortex over most of the upper surface aft of the rotation axis, resulting in a low-pressure area and producing a "nose-down" pitching moment (a negative C_m). The surface pressure coefficient (C_p) distribution for this particular time is shown in Fig. 15; as seen, the "positive" area of the pressure distribution aft of the quarter-chord is larger compared to that ahead of it, and hence a "nose-down" pitching moment.

On the other hand, during the downstroke at around the same angle, shown in Fig. 14(k), the flow over most of the upper surface is separated, resulting in a high-pressure area and producing a "nose-up" pitching moment, thus a positive C_m. The surface pressure coefficient distribution at this particular time is plotted in Fig. 16, which shows that the pressure on the upper surface is even higher than that on the lower surface aft of the quarter-chord. The net "positive" area of the pressure distribution aft of the quarter-chord is less than that ahead of it, hence, a "nose-up" pitching moment.

4.3.4. *Effect of pitch axis location*

If the pitch axis is located at the mid-chord ($x/c = 0.5$) rather than the quarter-chord ($x/c = 0.25$), the force and moment coefficients, averaged over the last two oscillation cycles, are as plotted in Fig. 13(c).

A comparison of the force coefficient loops for this case with those shown in Fig. 8(b), when the pitch axis is at the quarter-chord, suggests that moving the pitching axis location backwards does not have much effect on the force coefficients, but modifies significantly the pitching moment hysteresis loop. In this case a considerable increase in negative damping even at low reduced frequencies is observed.

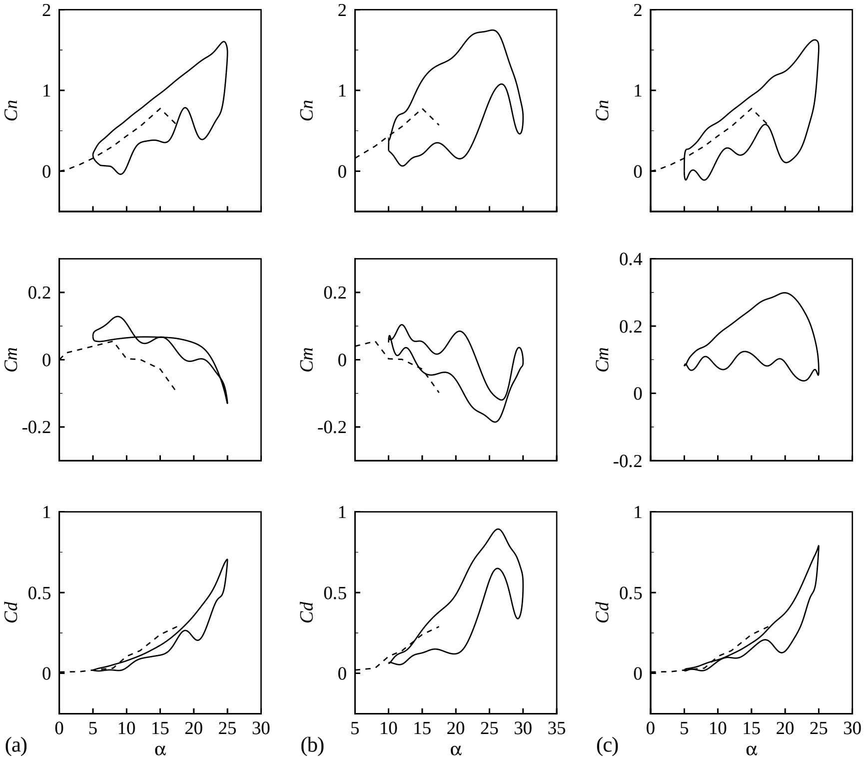

Fig. 13. The hysteresis loops for the normal force (C_n), pitching moment (C_m), and drag (C_d) coefficients for the airfoil oscillating with $\Delta\alpha = 10°$ and $\kappa = 0.25$, and: (a) $\bar{\alpha} = 15°$, Re = 3000, $x/c = 0.25$, (b) $\bar{\alpha} = 20°$, Re = 10^4, $x/c = 0.25$, (c) $\bar{\alpha} = 15°$, Re = 10^4, $x/c = 0.5$: ——, pitching case; - - -, steady case.

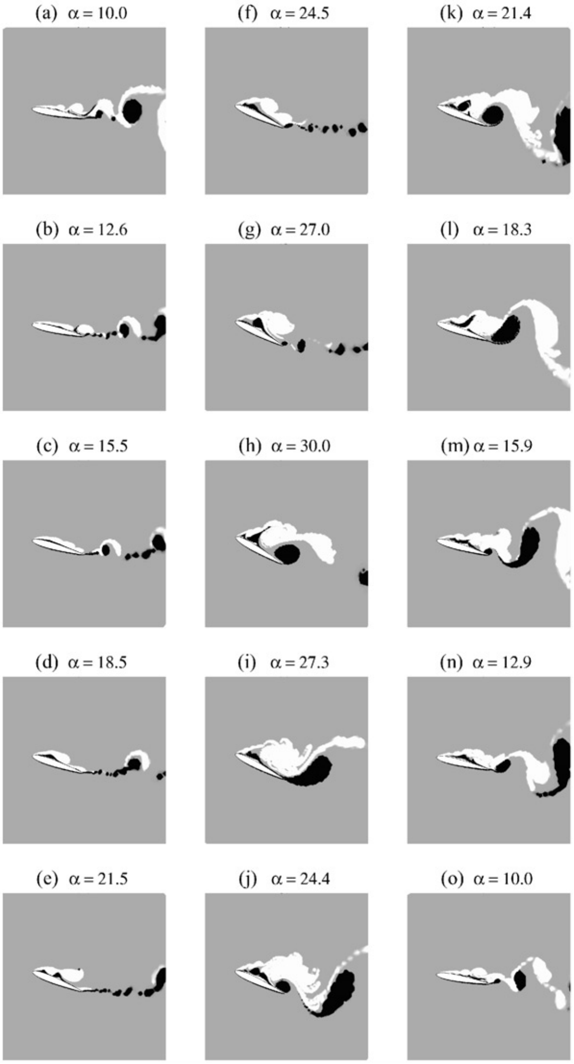

Fig. 14. Vorticity contour plots at several angles of attack for a pitching NACA 0012 airfoil, at $\kappa = 0.25$, $\Delta\alpha = 10^\circ$, $\bar{\alpha} = 20^\circ$, rotation axis at $c/4$, and $\text{Re} = 10^4$.

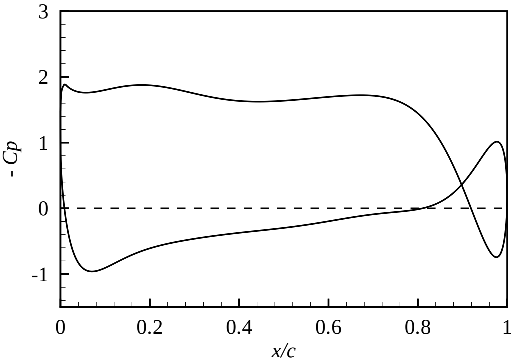

Fig. 15. The surface pressure coefficient distribution at $\alpha \simeq 21.5^\circ$ during the *upstroke* over the airfoil oscillating with $\kappa = 0.25$, $\Delta\alpha = 10^\circ$, $\bar{\alpha} = 20^\circ$, $x/c = 0.25$, and $\text{Re} = 10^4$.

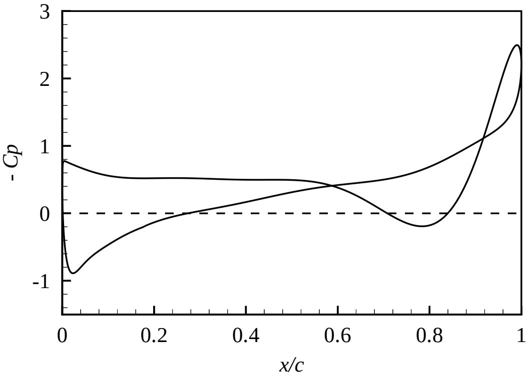

Fig. 16. The surface pressure coefficient distribution at $\alpha \simeq 21.5^\circ$ during the *downstroke* over the airfoil oscillating with $\kappa = 0.25$, $\Delta\alpha = 10^\circ$, $\bar{\alpha} = 20^\circ$, $x/c = 0.25$, and $\mathrm{Re} = 10^4$.

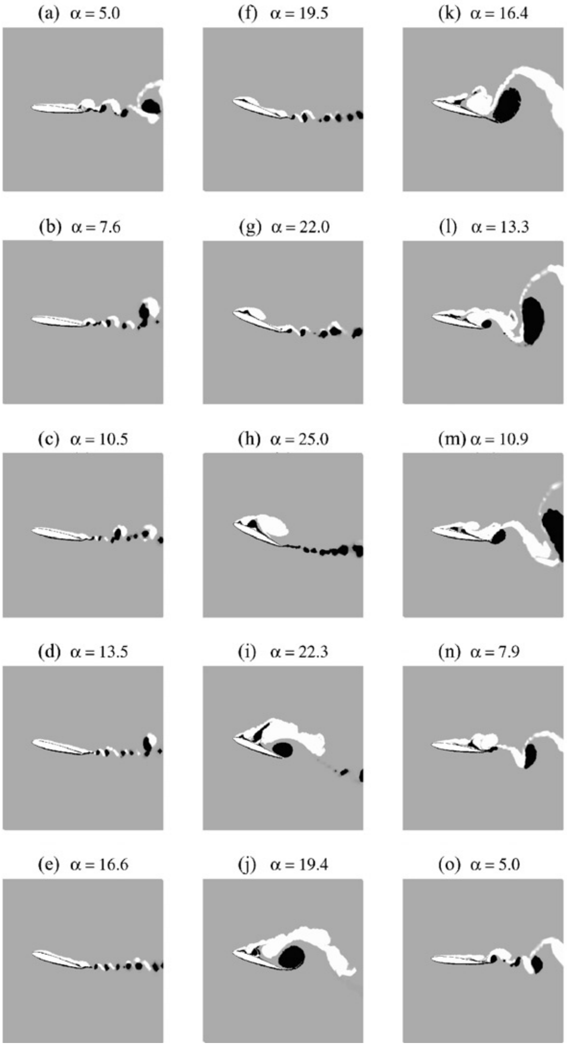

Fig. 17. Vorticity contour plots at several angles of attack for a pitching NACA 0012 airfoil, at $\kappa = 0.25$, $\Delta\alpha = 10^\circ$, $\bar{\alpha} = 15^\circ$, rotation axis at $c/2$, and $\mathrm{Re} = 10^4$.

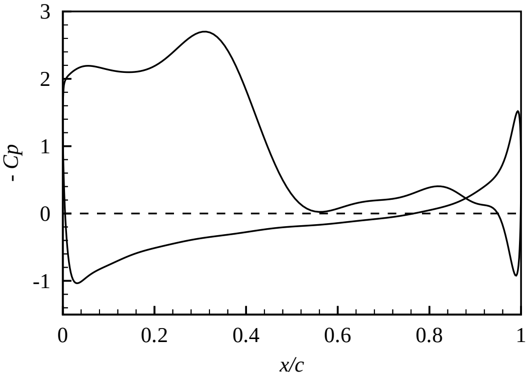

Fig. 18. The surface pressure coefficient distribution at $\alpha \simeq 19.5°$ during the *upstroke* over the airfoil oscillating with $\kappa = 0.25$, $\Delta\alpha = 10°$, $\bar{\alpha} = 15°$, $x/c = 0.25$, and $\mathrm{Re} = 10^4$.

The vorticity contour plots during the third oscillation cycle for the airfoil in this case, with $x/c = 0.5$, $\bar{\alpha} = 15°$, $\Delta\alpha = 10°$, and $\kappa = 0.25$, are shown in Fig. 17. The flow is attached over most of the upper surface of the airfoil at the beginning of the oscillation cycle, while the wake is still vortical due to the previous cycle. The flow remains attached during the upstroke up to $\alpha \approx 16.5°$, as was the situation with the pitch axis located at the quarter-chord. At $\alpha \approx 19.5°$ a separation bubble forms at the leading-edge which then develops into a vortex. At $\alpha_{\max}$ this leading-edge vortex has already travelled two-thirds of the airfoil upper surface.

In the downstroke part of the cycle a trailing-edge vortex forms, while the leading-edge vortex is being shed from the upper surface. As the downstroke continues the first trailing-edge vortex sheds, as seen in Fig. 17(k). Meanwhile, a second vortex forms on the upper surface, and is later shed from the surface. The flow starts to reattach at the leading-edge at $\alpha \approx 7.9°$. Even at $\alpha = 5°$, at the end of the cycle, the flow is not completely attached to the surface.

Comparing Fig. 17 with Fig. 11, with pitch axis located at the mid-chord and quarter-chord, respectively, shows that the flow fields in these two cases are very similar during most of the upstroke. Even at $\alpha_{\max}$ the two flow fields have considerable similarities. The most significant difference is in the timing of the formation and shedding of the trailing-edge vortices, which for $x/c = 0.5$ is slightly behind that for $x/c = 0.25$, as can be observed by comparing parts (k) with (m) of Figs. 17 and 11. The resemblance between the flow fields can also be detected from the similarities between the force coefficient plots of the two cases, shown in Figs. 8(b) and 13(c). However, the pitching moment coefficient loops for the two cases are quite different, which was predictable given the difference in location of the pitching axis. For $x/c = 0.5$ the pitching moment is always positive, which means that the aerodynamic center is always ahead of the pitch axis.[2]

The behavior of the pitching moment, as shown in Fig. 13(c), can be explained as follows. During most of the upstroke the flow is either attached near the leading-edge, or a vortex is present in this area. In either case a low-pressure region is maintained in this area. For example, at $\alpha \approx 19.5°$ the leading-edge vortex covers the front half of the upper surface, as seen Fig. 17(f). The surface pressure coefficient distribution for this instant of time is shown in Fig. 18. It can be seen that the pressure ahead of the mid-chord is much lower than that aft of the mid-chord, and thus a “nose-up” pitching moment about the mid-chord is produced. Also, during the downstroke the intensity of the separated flow is higher aft of the mid-chord, as seen in Fig. 17(j)–(n), keeping a lower pressure ahead of the mid-chord compared to that aft of the mid-chord. For example, Fig. 17(j) shows a large separated flow region aft of the mid-chord on the upper surface at $\alpha \approx 19.4°$ during the downstroke. The surface pressure coefficient distribution for this instant of time is shown in Fig. 19. It is clear that the pressure on the upper surface aft of the mid-chord is even higher than that on the lower surface. The pressure ahead of the mid-chord, on the other hand, is lower on the upper surface compared to that on the lower surface. Hence, a “nose-up” pitching moment is produced about the mid-chord. However, Figs. 18 and 19 show that the pressure on the upper surface ahead of the mid-chord is much lower (or, $-C_p$ is higher) during the upstroke compared to that during the downstroke, and hence, the positive pitching moment is higher during the upstroke.

---

[2] This, in turn, was predictable, since the aerodynamic center is usually located around the quarter-chord for most conventional airfoils.

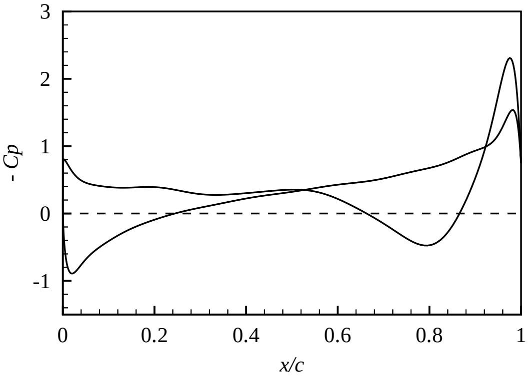

Fig. 19. The surface pressure coefficient distribution at $\alpha \simeq 19.4^\circ$ during the *downstroke* over the airfoil oscillating with $\kappa = 0.25$, $\Delta\alpha = 10^\circ$, $\bar{\alpha} = 15^\circ$, $x/c = 0.25$, and $\mathrm{Re} = 10^4$.

5. Conclusions

In this paper the pitching oscillations of a NACA 0012 airfoil were studied, and the effects of some parameters on the dynamic stall characteristics of the airfoil were investigated.

It was observed that the pitching oscillations of the airfoil delayed the flow separation to higher incidences compared to the static stall case. The normal force was observed to increase well beyond that at the static stall angle. Separation was observed to start from the leading-edge, followed by the formation and convection of a vortex along the surface of the airfoil. Trailing-edge vortices were also observed to form and shed from the airfoil. During the downstroke of the oscillation one or more ‘‘secondary’’ vortices were observed to form and release from the upper surface, following the release of the primary dynamic stall vortex.

The reduced frequency of oscillation was found to have a major effect on the flow field and the force coefficients of the airfoil. Flow separation was delayed to higher incidences with increasing reduced frequency. Hence, the peak in the normal force coefficient was observed at a higher angle of attack with increasing the reduced frequency. It was found that the maximum normal force slightly increased, and the minimum pitching moment decreased, with increasing reduced frequency. However, perhaps the most important effect due to an increase in the reduced frequency was a considerable increase in the ‘‘negative’’ damping in the pitching moment coefficient hysteresis loop observed at the highest reduced frequency.

The Reynolds number of the flow, on the other hand, was found to have little effect on the dynamic stall characteristics of the airfoil, at least for the range of $\mathrm{Re} = 3000\text{–}10^4$ considered in our simulations.

Increasing the mean incidence caused flow separation to occur earlier in an oscillation cycle, even at lower angles of attack compared to a case with a lower mean incidence. The flow field in this case was found to be more vortical, and the wake to be wider and more violent. Also, the hysteresis effects in the force and pitching moment coefficient loops intensified, and the maximum normal force and drag coefficients increased. On the other hand, the minimum pitching moment increased (its absolute value decreased), and the ‘‘negative’’ damping in the pitching moment loop was suppressed.

The simulations showed that moving the location of the pitch axis backwards, from the quarter-chord to the mid-chord, had minor effects on the flow field in terms of the flow separation and the timing of the formation and release of the leading- and trailing-edge vortices, as well as on the hysteresis loops of the force coefficients. For example, it was found that this change of location caused the trailing-edge vortex to be shed slightly later during the downstroke, the normal force coefficient loop to become slightly thinner, and the drag coefficient loop slightly wider. However, this change of the pitch axis location caused a dramatic change in the pitching moment loop: the pitching moment became positive during the entire cycle, and a large ‘‘negative’’ damping region appeared in the pitching moment loop. This behavior of the pitching moment loop was explained using the flow field information and the surface pressure coefficient distribution plots.

Acknowledgements

The authors gratefully acknowledge the financial support of the Natural Sciences and Engineering Research Council of Canada (NSERC) and Les Fonds FCAR du Québec.

References

Abbott, I.H., von Doenhoff, A.E., 1959. Theory of Wing Sections. Dover, New York.

Akbari, M.H., 1999. Bluff-body flow simulations using vortex methods. Ph.D. Thesis, McGill University, Montréal, Canada.

Akbari, M.H., Price, S.J., 2000. Simulation of the flow over elliptic airfoils oscillating at large angles of attack. Journal of Fluids and Structures 14, 757–777.

Carta, F.O., 1967a. An analysis of the stall flutter instability of helicopter rotor blades. Journal of the American Helicopter Society 12, 1–18.

Carta, F.O., 1967b. Unsteady normal force on an airfoil in a periodically stalled inlet flow. Journal of Aircraft 4, 416–421.

Chorin, A.J., 1973. Numerical study of slightly viscous flow. Journal of Fluid Mechanics 57, 785–796.

Crimi, P., 1973. Dynamic stall. AGARD-AG-172.

Ericsson, L.E., 1967. Comment on unsteady airfoil stall. Journal of Aircraft 4, 478–480.

Ericsson, L.E., Reding, J.P., 1971. Unsteady airfoil stall, review and extension. Journal of Aircraft 8, 609–616.

Ericsson, L.E., Reding, J.P., 1972. Dynamic stall of helicopter blades. Journal of the American Helicopter Society 17, 11–19.

Ericsson, L.E., Reding, J.P., 1980. Dynamic stall at high frequency and large amplitude. Journal of Aircraft 17, 136–142.

Ericsson, L.E., Reding, J.P., 1988. Fluid mechanics of dynamic stall. Part I: unsteady flow concepts. Journal of Fluids and Structures 2, 1–33.

Johari, H., Durgin, W.W., 1998. Direct measurement of circulation using ultrasound. Experiments in Fluids 25, 445–454.

Jumper, E.J., Huge, R.J., 1991. Simple theories of dynamic stall that are helpful in interpreting computational results. Computer Physics Communications 65, 158–163.

Lorber, P.F., Carta, F.O., 1988. Airfoil dynamic stall at constant pitch rate and high Reynolds number. Journal of Aircraft 25, 548–556.

Massey, B.S., 1979. Mechanics of Fluids, 4th Edition. Van Nostrand Reinhold, New York.

McCroskey, W.J., Carr, L.W., McAlister, K.W., 1976. Dynamic stall experiments on oscillating airfoils. AIAA Journal 14, 57–63.

Ohmi, K., Coutanceau, M., Phuoc Loc, T., Dulieu, A., 1991. Further experiments on vortex formation around an oscillating and translating airfoil at large incidences. Journal of Fluid Mechanics 225, 607–630.

Raffel, M., Kompenhans, J., Wernet, P., 1995. Investigation of the unsteady flow velocity field above an airfoil pitching under deep dynamic stall conditions. Experiments in Fluids 19, 103–111.

Tuncer, I.H., Wu, J.C., Wang, C.M., 1990. Theoretical and numerical studies of oscillating airfoils. AIAA Journal 28, 1615–1624.